

Deterministic Switching of Perpendicular Ferromagnets by Higher-order Spin-orbit Torque in Noncentrosymmetric Weyl Semimetals

Naomi Fokkens  ¹ and Fei Xue  ¹

¹*Department of Physics, University of Alabama at Birmingham, Birmingham, AL 35294, USA*

(Dated: November 18, 2025)

Field-free deterministic switching of perpendicular ferromagnets is a central challenge for spintronics applications, typically requiring explicit symmetry breaking. Here we show that deterministic switching can instead be achieved through higher-order (in magnetization angles) spin-orbit torques, even in systems that preserve in-plane mirror symmetry. Using a vector spherical harmonics expansion, we demonstrate that higher-order torque terms naturally give rise to additional out-of-equator fixed points, enabling reliable magnetization reversal when their magnitude is comparable to conventional lowest-order torques. We illustrate this mechanism with first-principles calculations on the noncentrosymmetric Weyl ferromagnet PrAlGe, where the combination of Weyl-node band topology and strong spin-orbit coupling produces sizable higher-order torque components. Because the Fermi surface is small, the conventional lowest-order torques are relatively weak, allowing the higher-order harmonics to compete on equal footing and strongly reshape the magnetization dynamics. The resulting spin dynamics confirm deterministic switching without additional symmetry breaking. Our results establish higher-order spin-orbit torque as a key ingredient for understanding and controlling magnetization dynamics in topological and spintronic materials.

I. INTRODUCTION

Realizing electric field control of magnetization without an external magnetic field is a central goal in spintronics applications such as magnetic random access memories and neuromorphic computing [1–4]. Spin-orbit torque (SOT) has emerged as a promising mechanism for such control [5, 6], requiring the coexistence of spin-orbit coupling, magnetization, and broken inversion symmetry. In prototypical heavy-metal/ferromagnet bilayers, an in-plane electric field can induce a spin current in the heavy metal layer that exerts a torque on the adjacent ferromagnet. Because the nonequilibrium spin accumulation can align with the magnetization for certain orientations, the torque vanishes in those cases, and its form is therefore strongly constrained by the underlying crystal symmetry.

In conventional bilayer systems with continuous rotational symmetry, the spin-orbit torque vanishes when the magnetization lies in-plane. As a result, ferromagnets with perpendicular magnetic anisotropy (PMA) exhibit non-deterministic switching: once the electric field is removed, the magnetization may relax either back to the original or into the reversed easy axis. This limitation is critical, since PMA is central for high-density, thermally stable spintronic devices [3, 7, 8]. The common strategy to achieve deterministic switching is to break in-plane mirror symmetry, either externally by applying an in-plane magnetic field [5, 9] or intrinsically by utilizing reduced-symmetry materials [10–14].

In this work, we demonstrate that the deterministic switching of ferromagnets with perpendicular magnetic anisotropy can be realized even *without* breaking in-plane mirror symmetry by incorporating higher-order (in magnetization angles) spin-orbit torque (SOT) terms. These symmetry-allowed contributions generate additional fixed points away from the equator, in contrast

to the conventional lowest-order torques that enforce only in-plane fixed points. Whether the magnetization relaxes to these out-of-equator states depends on the relative strength of higher- versus lower-order SOT terms. Using Landau-Lifshitz-Gilbert simulations of a minimal toy model containing both contributions, we construct a dynamical phase diagram that identifies the conditions under which deterministic switching occurs.

Higher-order SOTs naturally arise from strong spin-orbit coupling effects beyond the linear perturbative regime [15, 16]. To illustrate this mechanism in a real material, we consider the noncentrosymmetric Weyl ferromagnet PrAlGe [17–23], which exhibits both strong spin-orbit coupling and C_{4z} rotational symmetry. First-principles calculations reveal that higher-order SOT terms at the Fermi level are comparable in magnitude to conventional ones, enabling the deterministic switching without any additional symmetry breaking.

This paper is organized as follows. In Sec. II, we analyze the symmetry constraints on spin-orbit torque and express the allowed forms using vector spherical harmonics. In Sec. III, we construct a minimal toy model combining lower- and higher-order torques, and use Landau-Lifshitz-Gilbert simulations to map out the dynamical phase diagram, identifying the conditions for deterministic switching. Sec. IV presents first-principles calculations of spin-orbit torques in PrAlGe, followed in Sec. V by an analysis of the resulting spin dynamics and the role of higher-order contributions in producing both deterministic reversal and sustained precession. Finally, Sec. VI summarizes the conclusions, discusses experimental relevance, and outlines future directions for exploring higher-order torque effects.

II. SYMMETRY-ALLOWED SPIN-ORBIT TORQUE

In rotationally symmetric systems with broken inversion symmetry (with the symmetry-breaking direction denoted $\hat{\mathbf{n}}$), the lowest-order spin-orbit torques take two characteristic forms [24–26]: $\hat{\mathbf{p}} \times \hat{\mathbf{m}}$ and $\hat{\mathbf{m}} \times (\hat{\mathbf{p}} \times \hat{\mathbf{m}})$, where $\hat{\mathbf{p}} = \hat{\mathbf{n}} \times \hat{\mathbf{E}}$. As illustrated in Fig. 1 (a,b) for $\hat{\mathbf{n}} = \hat{\mathbf{z}}$, these correspond to the conventional fieldlike and dampinglike torques. Their angular dependence resembles that of a static magnetic field and a Landau-Lifshitz damping term, respectively. Together, they stabilize an in-plane fixed point on the equator, $\hat{\mathbf{m}} = \hat{\mathbf{p}}$, where the total torque vanishes.

For field-free deterministic switching of perpendicular ferromagnets, the torque must drive the magnetization from its initial easy axis to the opposite axis under an applied electric field. This requires the existence of a stable fixed point *off* the equator in the opposite hemisphere, so that once the field is removed, the magnetization relaxes into the reversed easy-axis state. Reversing the polarity of the electric field then drives the magnetization back, enabling fully bidirectional control solely through the applied field.

In systems with full rotational symmetry, however, all lowest-order spin-orbit torques vanish when $\hat{\mathbf{m}}$ lies in-plane, preventing the formation of off-equator fixed points. One approach is to break an in-plane mirror symmetry so that $\hat{\mathbf{p}}$ acquires an out-of-plane component [10, 11]. Yet even in materials such as Fe_3GeTe_2 , which intrinsically breaks an in-plane mirror symmetry, lowest-order spin-orbit torques still stabilize only equatorial fixed points [27]. As shown in Ref. [26], off-equator fixed points appear only when higher-order, magnetization-dependent torque terms are included. These observations motivate the central question of this work: whether higher-order spin-orbit torques, without explicitly breaking any in-plane symmetry, can generate off-equator fixed points that enable deterministic switching of a perpendicular ferromagnet.

To answer this, we systematically derive the symmetry-allowed forms of spin-orbit torque, using a vector spherical harmonics expansion [25, 26, 28]. Unlike conventional Cartesian expansions, this formalism provides a complete orthonormal basis without introducing artificial cutoffs and naturally separates torques into fieldlike and dampinglike components. In addition, it offers a transparent way to identify and classify higher-order contributions consistent with the crystal symmetry, making it particularly suited for the present study.

We focus on systems with C_{4z} symmetry, with both xz and yz mirror planes. This choice isolates higher-order torque effects: unlike C_{3z} or other lower-symmetry groups, C_{4z} does not break any in-plane mirror symmetry, and unlike continuous rotational symmetry, it does not forbid azimuthal angular dependence [25]. Thus C_{4z} is the minimal symmetry setting where higher-order torques can be unambiguously disentangled from symme-

try breaking.

The spin-orbit torque is described in linear response by $\mathcal{T}_i = \tau_{ij} E_j$, where spin-orbit torque tensor can be expanded in vector spherical harmonics following the methodology of Ref. [26], with system-specific details given in Appendix A. Applying this expansion under the symmetry constraints for an electric field along $\hat{\mathbf{x}}$ yields the allowed higher-order torque components, which separate naturally into time-reversal even and odd contributions:

$$\begin{aligned} \boldsymbol{\tau}^{\text{even}}(\hat{\mathbf{x}}) = & \sum_{l,m} [C_{2l,4m\pm 1}^{\text{F}} \text{Re } \mathbf{Y}_{2l,4m\pm 1}^{\text{F}} \\ & + C_{2l+1,4m\pm 1}^{\text{D}} \text{Im } \mathbf{Y}_{2l+1,4m\pm 1}^{\text{D}}], \end{aligned} \quad (1)$$

$$\begin{aligned} \boldsymbol{\tau}^{\text{odd}}(\hat{\mathbf{x}}) = & \sum_{l,m} [C_{2l,4m\pm 1}^{\text{D}} \text{Re } \mathbf{Y}_{2l,4m\pm 1}^{\text{D}} \\ & + C_{2l+1,4m\pm 1}^{\text{F}} \text{Im } \mathbf{Y}_{2l+1,4m\pm 1}^{\text{F}}]. \end{aligned} \quad (2)$$

Equations 1 and 2 consist of a symmetry-allowed combination of fieldlike and dampinglike terms, with coefficients C specifying the weight of each contribution. For an electric field applied along $\hat{\mathbf{y}}$, the corresponding torque forms follow directly from Eqs. 1-2 by applying the C_{4z} rotational symmetry. The explicit expressions are provided in Appendix A.

The symmetry-allowed forms of spin-orbit torque are illustrated in Fig. 1. Panels (a) and (b) show the conventional lowest-order fieldlike and dampinglike terms, which enforce only equatorial fixed points. Panels (c)-(h) present representative examples of higher-order torques permitted by C_{4z} symmetry. In each plot, arrows indicate the torque direction and the color scale denotes magnitude, with blue regions corresponding to vanishing torque and thus potential fixed points. Because the vector spherical harmonics expansion includes contributions of arbitrarily high order, only a subset of symmetry-allowed terms relevant for the present analysis is shown here. In the next section, we examine the dynamical consequences of selected higher-order terms by constructing a minimal toy model, which highlights how these contributions modify fixed points and enable deterministic switching.

III. DETERMINISTIC SWITCHING IN A LANDAU-LIFSHITZ-GILBERT MODEL WITH HIGHER-ORDER TORQUES

Having established the symmetry-allowed forms of spin-orbit torque, we next examine their dynamical consequences using a minimal Landau-Lifshitz-Gilbert (LLG) model. Our goal is to identify the simplest combination of torque harmonics capable of producing deterministic magnetization reversal in a system that preserves global C_{4z} and mirror symmetries. We focus on a minimal torque expansion

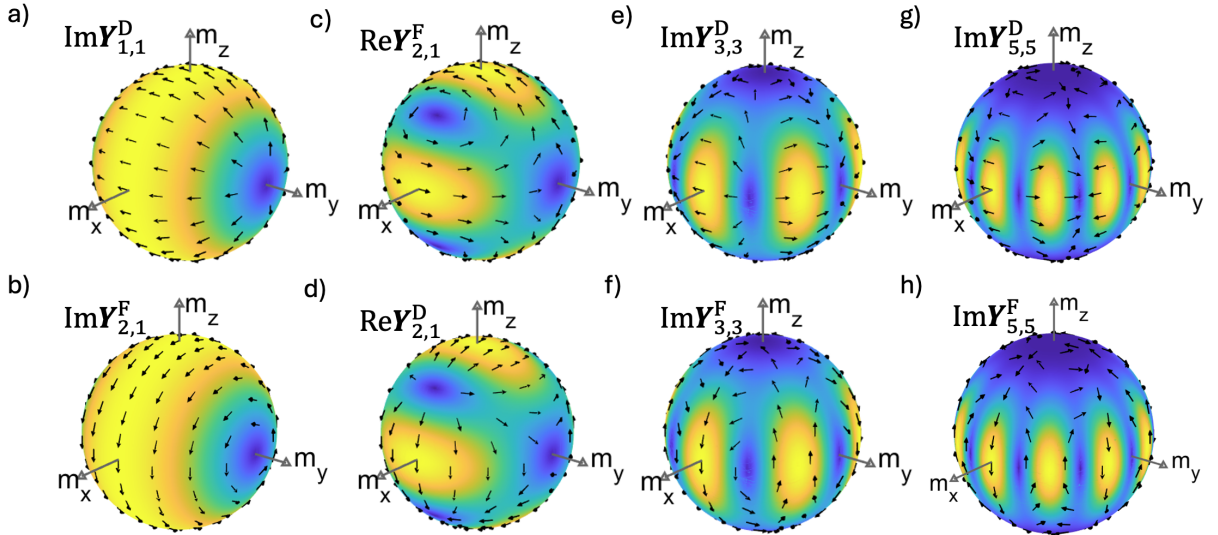


FIG. 1. Angular dependence of representative spin-orbit torque components for an applied electric field along \hat{x} . Arrows indicate the torque direction on the unit sphere of magnetization $\hat{\mathbf{m}}$, while the color scale denotes torque magnitude. Panels (a) and (b) show the conventional lowest-order dampinglike ($\text{Im } \mathbf{Y}_{1,1}^D \propto \hat{\mathbf{m}} \times (\hat{\mathbf{y}} \times \hat{\mathbf{m}})$) and fieldlike ($\text{Im } \mathbf{Y}_{1,1}^F \propto \hat{\mathbf{y}} \times \hat{\mathbf{m}}$) torques, which stabilize only equatorial fixed points. Panels (c)-(h) illustrate selected higher-order symmetry-allowed torques, including $\text{Re } \mathbf{Y}_{2,1}^F$, $\text{Re } \mathbf{Y}_{2,1}^D$, $\text{Im } \mathbf{Y}_{3,3}^D$, $\text{Im } \mathbf{Y}_{3,3}^F$, $\text{Im } \mathbf{Y}_{5,5}^D$, and $\text{Im } \mathbf{Y}_{5,5}^F$. Regions in blue correspond to vanishing torque, indicating fixed points. These higher-order contributions introduce off-equator fixed points that play a crucial role in enabling deterministic switching when comparable in strength to the conventional terms.

$$\boldsymbol{\tau} = \text{Im } \mathbf{Y}_{1,1}^D + \text{Im } \mathbf{Y}_{1,1}^F + \text{ratio} * \text{Im } \mathbf{Y}_{3,3}^F. \quad (3)$$

The first two terms, $\text{Im } \mathbf{Y}_{1,1}^D$ and $\text{Im } \mathbf{Y}_{1,1}^F$, represent the conventional lowest-order dampinglike and fieldlike torques, which are expected to dominate magnetization dynamics. They generate fixed points confined to the $\mathbf{m} \parallel \hat{\mathbf{y}}$, as shown in Fig. 1 (a-b). In this situation a dc electric field cannot uniquely steer the magnetization from $+\hat{\mathbf{z}}$ to a definite state in the opposite hemisphere. Depending sensitively on small perturbations, the magnetization either returns to the original side or relaxes to the opposite easy-axis (nondeterministic switching).

Introducing higher-order angular harmonics ($\ell > 1$) adds additional fixed points off the equator [Figs. 1(c-h)], but they appear symmetrically in both hemispheres due to the preserved mirror symmetries σ_{xz} and σ_{yz} , leaving the dynamics degenerate. The key question, then, is whether the combined torque field drives $\hat{\mathbf{m}}$ toward a same-hemisphere fixed point (no switching) or across the equator into its mirror-related counterpart (deterministic switching).

A crucial ingredient is the inclusion of a higher-order term with a different azimuthal structure, such as $\text{Im } \mathbf{Y}_{3,3}^F$ [Fig. 1(f)]. Unlike the conventional $m = 1$ torques, which generate single-lobed angular patterns, this $m = 3$ component redistributes the torque on the unit sphere so that the flow lines naturally cross the equator rather than remaining trapped within one hemisphere. When combined with the $m = 1$ torques, it modifies the global

flow on the unit sphere: trajectories starting near $+\hat{\mathbf{z}}$ are guided toward a unique off-equator fixed point in the opposite hemisphere, while those starting near $-\hat{\mathbf{z}}$ relax toward its mirror-related partner. Importantly, the torque still vanishes at $\hat{\mathbf{m}} = \pm \hat{\mathbf{y}}$ by mirror symmetry, so deterministic switching only occurs when the initial magnetization lies away from this high-symmetry direction.

The magnetization dynamics in our toy model are governed by the Landau-Lifshitz-Gilbert (LLG) equation [29]:

$$\frac{d\hat{\mathbf{m}}}{dt} - \alpha \hat{\mathbf{m}} \times \frac{d\hat{\mathbf{m}}}{dt} = -\gamma \mu_0 H_A (\hat{\mathbf{m}} \times \hat{\mathbf{z}}) (\hat{\mathbf{m}} \cdot \hat{\mathbf{z}}) + \mathcal{T} \quad (4)$$

where $\hat{\mathbf{m}}$ denotes the magnetization direction, γ is the gyromagnetic ratio, $\hat{\mathbf{z}}$ specifies the easy axis and \mathcal{T} represents the spin-orbit torque. In the simulations, the damping parameter is fixed at $\alpha = 0.01$, and the anisotropy field is set to $H_A = 2$ T, oriented along the perpendicular $\hat{\mathbf{z}}$ direction.

Figure 2 summarizes the numerical results of the toy model. Panel (a) shows the case of a relatively small ratio (0.1) of higher-order torque contributions to the conventional lowest-order terms. In this regime, the magnetization is driven only to the symmetry-enforced fixed point at the equator, resulting in nondeterministic switching. In contrast, panel (b) illustrates the case of a larger ratio (0.4) of higher-order to lowest-order terms. Here, the magnetization crosses the equator and settles into a new stable off-equator fixed point created by the higher-order torques. When the electric field is

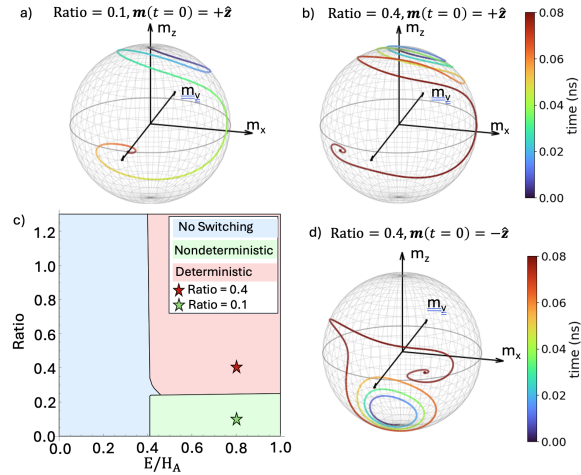


FIG. 2. LLG simulations of magnetization dynamics with conventional lowest-order torques [Fig. 1(a,b)] and the selected higher-order torque component [Fig. 1(f)]. Panels (a) and (b) show representative trajectories for ratios of higher-to lower-order torque amplitudes of 0.1 and 0.4, respectively. For a small ratio (a), the magnetization is driven to the equatorial fixed point, resulting in nondeterministic switching. For a larger ratio (b) the trajectory crosses the equator and relaxed into a reversed state, demonstrating deterministic switching. Panel (c) presents the phase diagram of switching regimes—deterministic, nondeterministic, and no switching—as functions of the applied electric field E relative to the anisotropy field H_A and the ratio of higher-order contributions. Panel (d) shows that starting from the south pole, the same electric-field direction drives the magnetization to the symmetry-related north-hemisphere fixed point, illustrating symmetry-preserving deterministic switching without reversing the field polarity.

removed, the magnetization reliably relaxes into the reversed easy-axis direction, thereby realizing deterministic switching. Panel (c) presents a phase diagram mapping the switching regimes—deterministic, nondeterministic, and no switching—as functions of the applied electric field strength (E) relative to the anisotropy field (H_A) and the relative weight (“ratio”) of higher-order torque terms.

Importantly, this deterministic switching mechanism is not unique to the specific $\text{Im}\mathbf{Y}_{3,3}^F$ term used in the toy model. Other higher-order harmonics with different azimuthal structures can generate similar behavior: for instance, the DFT-derived torque coefficients in PrAlGe presented later in Sec. V show that $\text{Im}\mathbf{Y}_{5,5}^D$ is sufficiently large to induce deterministic switching under realistic conditions, while additional components can lead to oscillatory dynamics (see Appendix C). This generality underscores that deterministic switching does not rely on a single harmonic, but on the interplay between conventional and higher-order torque symmetries that promote magnetization flow across the equator.

Finally, this “symmetry-preserving” switching mechanism differs fundamentally from the conventional

symmetry-breaking case. In broken-mirror systems, reversing the magnetization between north and south poles requires reversing the electric-field direction, as each field polarity favors only one hemisphere (governed by mirror σ_{yz} symmetry). Here, by contrast, the same field direction drives reversal from either pole [Fig. 2(d)]: an initial state and its mirror partner (related by σ_{xz} mirror symmetry: $\theta \rightarrow \pi - \theta$, $\phi \rightarrow \pi - \phi$) evolve toward final states that are themselves mirror related. Reversing the field still reverses the switching trajectory, but now the magnetization is driven toward a different fix point related by the σ_{yz} mirror. Thus deterministic switching arises not from breaking symmetry but from the internal angular structure of the spin-orbit torque itself.

IV. FIRST-PRINCIPLES ELECTRONIC STRUCTURE AND WANNIERIZATION OF PRALGE

Motivated by the symmetry analysis and toy model results, we now turn to PrAlGe, a noncentrosymmetric ferromagnetic Weyl semimetal from the *RAI*Ge family that provides an ideal platform to test the role of higher-order spin-orbit torques. PrAlGe possesses C_{4z} rotational symmetry, simultaneously breaks time-reversal and inversion symmetries (stabilizing Weyl nodes), and exhibits strong spin-orbit coupling, making it a promising candidate for spintronic applications [17, 19, 20]. These properties suggest that higher-order torque contributions may be sizable, and if comparable to the lowest-order terms, could enable deterministic switching consistent with the toy model predictions.

To evaluate spin-orbit torques in PrAlGe, we first construct a reliable electronic structure model based on density functional theory (DFT). PrAlGe crystallizes in the noncentrosymmetric tetragonal space group $I4_{1md}$ (No. 109), which preserves C_{4z} rotational symmetry. Calculations are performed within the GGA+ U [30] framework using VASP [31] [32] [33] (computational parameters are given in Appendix D). A Hubbard $U = 4$ eV is applied to the Pr f -orbitals, consistent with prior studies [17, 19], which effectively shifts the localized f states away from the Fermi level [Fig. 3(b)]. This ensures that the low-energy electronic structure is dominated by itinerant spd states, providing a reasonable basis for transport and torque modeling. Both collinear and noncollinear calculations are carried out, and the resulting crystal structure, density of states, and band dispersions [Figs. 3(a-d)] are consistent with earlier studies of the *RAI*Ge family [17, 19]. In particular, the band structure shows the expected semimetallic character with linearly dispersing crossings near the Fermi level that evolve into Weyl points when spin-orbit coupling and ferromagnetism are included, in agreement with prior reports.

From the collinear DFT results, we construct a tight-binding model using Wannier90 [34] and symmetrize it with WannSymm [35] to enforce the crystal symmetry.

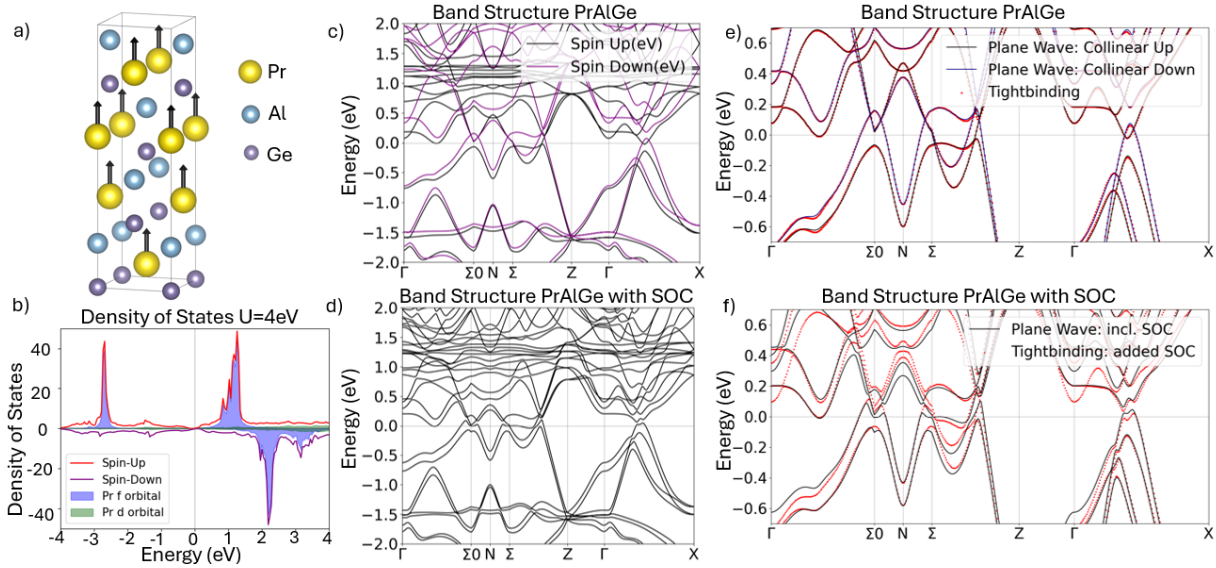


FIG. 3. (a) Crystal structure of PrAlGe with out-of-plane Pr magnetic moments. (b) Spin-resolved density of states calculated with Hubbard $U = 4$ eV, highlighting the Pr f orbitals. (c,d) Electronic band structures of PrAlGe from plane-wave DFT: (c) collinear calculation without spin-orbit coupling (SOC) and (d) noncollinear calculation including SOC. (e) Comparison of symmetrized Wannier-interpolated bands with the collinear plane-wave results (c). (f) Comparison of Wannier-interpolated bands with SOC added at the atomic level to the collinear model, benchmarked against the noncollinear plane-wave results (d). Panels (e,f) are shown in a reduced energy range near the Fermi level to highlight the quality of the Wannier fitting.

The Wannier-interpolated bands reproduce the collinear DFT dispersion near the Fermi level [Fig. 3(e)]. Spin-orbit coupling is then included as an on-site $\alpha\mathbf{L} \cdot \mathbf{S}$ term [36, 37] and benchmarked against the noncollinear DFT results [Fig. 3(f)]. This procedure is advantageous because Wannierization of the collinear Hamiltonian is more stable and keeps the exchange term purely spinlike, enabling straightforward rotation of the magnetization in torque calculations. At the same time, the atomic SOC approach reproduces the essential band features of the noncollinear calculation, providing a reliable model for analyzing spin-orbit torque and its angle dependence.

This Wannier-based model captures the essential electronic and spin-dependent properties of PrAlGe. In particular, Appendix F confirms that the Weyl points obtained from the noncollinear VASP calculations are faithfully reproduced in the symmetrized tight-binding model with atomic SOC, ensuring that no topological features are lost in the fitting procedure. This agreement provides a robust foundation for calculating spin-orbit torques and quantifying the magnitude of higher-order torque components.

V. SPIN DYNAMICS AND DETERMINISTIC SWITCHING IN PRALGE

With the validated Wannier tight-binding Hamiltonian in hand, we now turn to the calculation of spin-orbit torques and the resulting magnetization dynamics. Using the symmetry framework established in Sec. II,

the torque is expanded in a vector spherical harmonics basis, allowing us to decompose the contributions into lowest-order (conventional) and higher-order components. We then analyze how these torques govern magnetization dynamics in PrAlGe by solving the Landau-Lifshitz-Gilbert (LLG) equation, directly connecting the symmetry-allowed torque terms to the possibility of deterministic switching.

The standard Kubo formula [26, 38–40] is used to evaluate the time-reversal even and odd components of the spin-orbit torque in PrAlGe, based on the *ab initio* tight-binding Hamiltonian constructed in Sec. IV:

$$\tau_{ij}^{\text{even}} = 2e \sum_{\mathbf{k}, n, m \neq n} f_{n\mathbf{k}} \frac{\text{Im} \langle \psi_{n\mathbf{k}} | \frac{\partial H_{\mathbf{k}}}{\partial k_j} | \psi_{m\mathbf{k}} \rangle \langle \psi_{m\mathbf{k}} | \mathcal{T}_i | \psi_{n\mathbf{k}} \rangle}{(E_{m\mathbf{k}} - E_{n\mathbf{k}})^2 + \eta^2}, \quad (5)$$

$$\tau_{ij}^{\text{odd}} = \frac{e}{\pi} \sum_{\mathbf{k}, n, m} \frac{\eta^2 \text{Re} \left[\langle \psi_{n\mathbf{k}} | \mathcal{T}_i | \psi_{m\mathbf{k}} \rangle \langle \psi_{m\mathbf{k}} | \frac{\partial H_{\mathbf{k}}}{\partial k_j} | \psi_{n\mathbf{k}} \rangle \right]}{[(\mu - E_{n\mathbf{k}})^2 + \eta^2] [(\mu - E_{m\mathbf{k}})^2 + \eta^2]}. \quad (6)$$

Here $|\psi_{n\mathbf{k}}\rangle$ are the Bloch eigenstates of the Hamiltonian $H_{\mathbf{k}}$, $E_{n\mathbf{k}}$ are the corresponding band energies, and $f_{n\mathbf{k}}$ is the Fermi-Dirac function evaluated at the chemical potential μ . The torque operator is defined as $\mathcal{T} = -\frac{i}{\hbar} [\Delta \cdot \hat{\mathbf{S}}, \hat{\mathbf{S}}]$, where $\hat{\mathbf{S}}$ is the spin operator and Δ is the time-reversal odd exchange-correlation field that couples to spin. The indices i, j denote the directions of torque and the applied electric field, respectively. The

$C_{1,1}^D$	$C_{3,1}^D$	$C_{3,3}^D$	$C_{5,5}^D$	$C_{2,1}^D$	$C_{1,1}^F$	$C_{3,3}^F$
-0.022	0.022	0.012	0.024	0.023	0.027	-0.008

TABLE I. The table shows the coefficients of the fitting for significant spin-orbit torque with units ea_0/\hbar at $\mu = 0.02$ eV. The first four are time-reversal even components while the last three are time-reversal odd components. The coefficients less than 0.01 are dropped here for brevity.

parameter η is the Lorentzian broadening used to model disorder and finite-temperature smearing (here we use $\eta = 25$ meV, $k_B T = 1.6$ meV).

We then project the *ab initio* torques onto the symmetry-allowed vector spherical harmonics forms of Eqs. 1 and 2. As expected, the extracted coefficients respect the C_{4z} symmetry of PrAlGe, with only symmetry-allowed terms remaining. To assess the relative importance of different torque harmonics, it is useful to examine how the fitted coefficients $C_{\ell,m}(\mu)$ evolve as the chemical potential is varied. In any metallic system the spin-orbit torque is an energy-dependent quantity, and scanning μ provides a systematic way to identify regimes where the higher-order components become comparable to the conventional lowest-order terms. The resulting trends are shown in Fig. 4. Panel (a) illustrates that the conventional lowest-order terms $C_{1,1}^D$ and $C_{1,1}^F$ are suppressed near the Fermi level, while panel (b) shows that several higher-order components—notably the dampinglike $C_{5,5}^D$ and, to a lesser extent, the fieldlike $C_{3,3}^F$ and dampinglike $C_{3,3}^D$ —become comparable in magnitude over the range $\mu \approx 0\text{--}0.1$ eV.

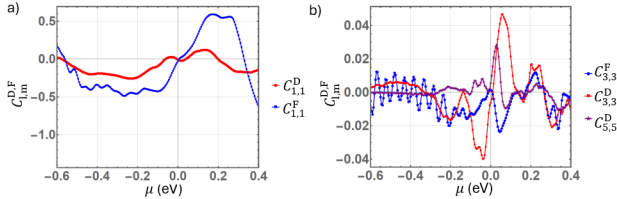


FIG. 4. Dependence of selected vector spherical harmonics coefficients on chemical potential μ . (a) Conventional lowest-order terms $C_{1,1}^D$ and $C_{1,1}^F$. (b) Dominant higher-order terms $C_{3,3}^F$, $C_{3,3}^D$, and $C_{5,5}^D$.

Importantly, the fitted coefficients at $\mu = 0.02$ eV (Table I) reveal that higher-order terms make contributions comparable in magnitude to the conventional components. We see that the higher-order harmonic emphasized in the toy model, $\text{Im } \mathbf{Y}_{3,3}^F$, is present but relatively small. Instead, the dampinglike $\text{Im } \mathbf{Y}_{5,5}^D$ term is the dominant higher-order contribution. As shown in the full torque field (Fig. 5) and confirmed by the phase-diagram analysis in Appendix C, a sufficiently large $\text{Im } \mathbf{Y}_{5,5}^D$ produces the similar off-equator fixed-point structure and deterministic-switching behavior identified in the toy model. This establishes $\text{Im } \mathbf{Y}_{5,5}^D$ as the key higher-order component governing the switching dynam-

ics in PrAlGe.

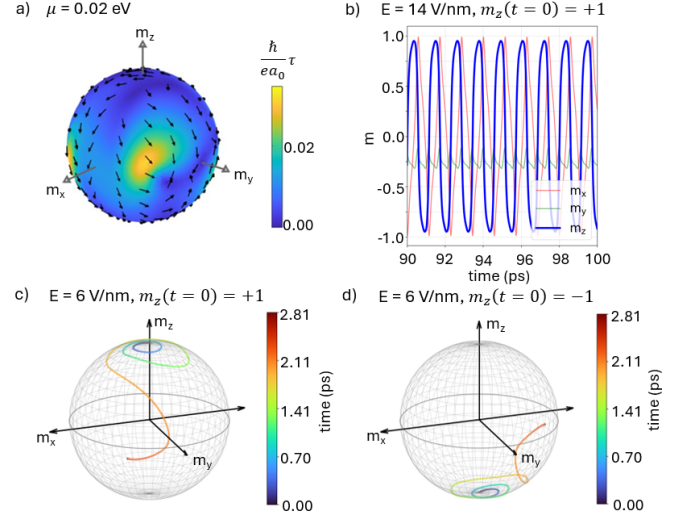


FIG. 5. Angular dependence of spin-orbit torque in PrAlGe at $\mu = 0.02$ eV. (a) spin-orbit torque in units $\frac{\hbar}{ea_0}$, evaluated for an applied electric field along \hat{x} . a_0 is the atomic Bohr radius. The color scale indicates the torque magnitude on the magnetization unit sphere, while arrows denote the torque direction. (c,d) Magnetization trajectories obtained by solving the LLG equation with the *ab initio* torque of panel (a) for $E \parallel \hat{x}$, starting from initial states in the (c) northern and (d) southern hemispheres at the same electric field. Trajectories are drawn on the unit sphere; color encodes time. (b) For a larger electric field than in (c,d), the magnetization no longer relaxes to the off-equator fixed points but instead exhibits sustained precessional oscillations. The oscillation frequency is tunable with electric-field strength; for $E = 14$ V/nm the frequency is approximately 0.85 THz.

The calculated even and odd spin-orbit torques are combined and plotted on the magnetization unit sphere in Fig. 5(a), revealing the full angular dependence of the SOT in PrAlGe. In contrast to the conventional lowest-order fieldlike and dampinglike forms in Fig. 1(a,b), the resulting spin-orbit torque exhibits pronounced higher-order angular structures with off-equator fixed points. The overall magnitude of the torque is relatively small compared to conventional bilayer system [11, 38], consistent with the reduced density of states near the Fermi level in this Weyl semimetal. But its angular profile is qualitatively different: the higher-order harmonics identified above—most notably the dampinglike $\text{Im } \mathbf{Y}_{5,5}^D$ term—substantially reshape the torque field. As shown below, this modified phase portrait is precisely what enables deterministic switching in PrAlGe.

To assess the dynamics, we solve the Landau-Lifshitz-Gilbert equation using the fitted torque coefficients and the DFT-derived uniaxial anisotropy field for PrAlGe, $\mu_0 H_A = 47.9$ T (consistent with prior estimates [41]), and a damping parameter $\alpha = 0.01$. We note that this H_A is large; DFT often overestimates 4f magnetocrystalline anisotropy, and recent measurements [42, 43] in-

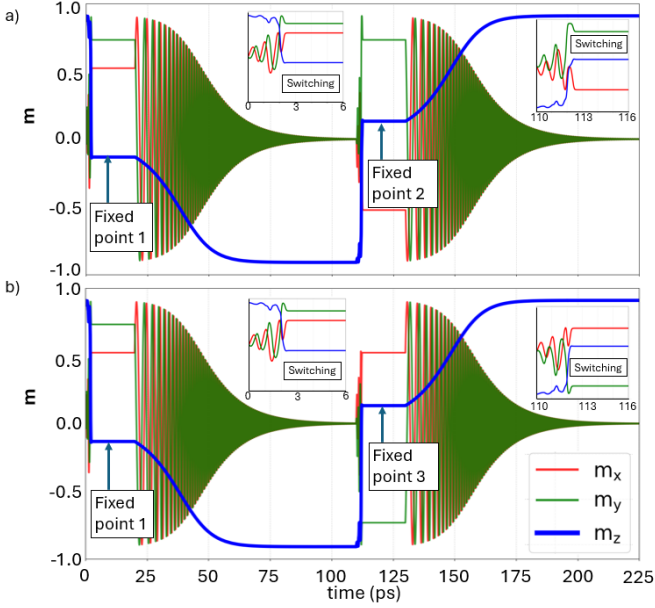


FIG. 6. Reversible switching protocol using two electric-field pulses. Time evolution of the magnetization components (m_x, m_y, m_z) under successive pulses of $\mathbf{E} \parallel \hat{\mathbf{x}}$, with relaxation intervals in between. In both panels the system starts near $+m_z$, is driven to an off-equator fixed point (labeled “Fixed point 1”), and relaxes to $-m_z$ after the first pulse is turned off. In panel (a), a second pulse with the same polarity then drives the magnetization to a different off-equator fixed point in the northern hemisphere (“Fixed point 2”), from which it relaxes back to $+m_z$ when the field is removed. In panel (b), the second pulse has the opposite polarity and accesses a third mirror-related fixed point in the northern hemisphere (“Fixed point 3”). Insets show the short-time switching dynamics to each fixed point. In both cases the protocol yields deterministic $+m_z \leftrightarrow -m_z$ switching, but through different fixed points.

dicate a strong Ising-like anisotropy with hard-axis saturation fields of at least several tesla (order 5 – 30 T). These parameters primarily set the electric-field scale (and timescale) required for switching. Crucially, varying H_A or α does not change the qualitative phase portrait: the higher-order torque components still create off-equator fixed points that enable deterministic switching once the threshold condition is met.

The resulting spin dynamics are shown in Fig. 5(c,d). For an electric field applied along $\hat{\mathbf{x}}$, a magnetization starting in the northern hemisphere relaxes toward a stable off-equator fixed point below the equator, while a magnetization starting in the southern hemisphere relaxes toward its mirror partner above the equator. By contrast, when the electric field is increased beyond the deterministic window [Fig. 5(b)], the dynamics enter a strongly precessional regime in which the magnetization oscillates around the fixed points rather than relaxing to them.

To illustrate how deterministic switching behavior [Fig. 5(c), (d)] enables reversible control of the perpendic-

ular magnetization, we apply a sequence of two electric-field pulses and let the magnetization relax in between, as shown in Fig. 6. In both panels the magnetization is initially prepared near $+m_z$ and the first pulse $\mathbf{E} \parallel \hat{\mathbf{x}}$ drives it toward an off-equator fixed point in the opposite hemisphere within 10 ps (fast switching dynamics are shown in insets). When the field is turned off, the magnetization relaxes to the $-m_z$ easy axis. A second pulse then returns the system to the opposite hemisphere, but at different fixed points depending on the pulse polarity. In Fig. 6(a) the two pulses have the same sign, and the magnetization visits two distinct off-equator fixed points that are symmetrically related as $(m_x, m_y, m_z) \rightarrow (-m_x, m_y, -m_z)$. In Fig. 6(b) the second pulse has the opposite sign (like the conventional symmetry breaking case), and the trajectory instead visits another fixed point related by $(m_x, m_y, m_z) \rightarrow (m_x, -m_y, -m_z)$. Thus the dynamics access three symmetry-related fixed points, (m_x, m_y, m_z) , $(-m_x, m_y, -m_z)$, and $(m_x, -m_y, -m_z)$, and in all cases the system is deterministically switched between $+m_z$ and $-m_z$. The key distinction from conventional symmetry-breaking schemes is that both same-polarity and opposite-polarity pulses can realize reversible switching, while landing in different mirror-related fixed points on the magnetization sphere.

VI. DISCUSSION

In this work, we demonstrate a robust and symmetry-guided mechanism for deterministic switching driven by higher-order spin-orbit torques using both toy models and a real material. Although PrAlGe is a complex material with strongly correlated f electrons and multiple electronic bands near the Fermi level, our *ab initio* calculations show that it naturally realizes the key condition identified in the toy model: the higher-order harmonics become comparable in magnitude with the lowest-order torque components that are suppressed over an energy window. In this regime the torque field develops symmetry-allowed off-equator fixed points, enabling deterministic switching of the perpendicular magnetization order parameter without requiring explicit symmetry breaking.

Although we illustrate the switching mechanism using $\mu = 0.02$ eV, where the higher-order harmonics are particularly pronounced, we emphasize that deterministic trajectories are not unique to this choice. As shown in Fig. 4, the relative strength of higher-order terms varies smoothly with chemical potential, and several nearby values of μ also yield torque fields with off-equator fixed points. The mechanism is therefore not fine-tuned to a single energy, but persists across a finite window of band filling, further underscoring its robustness.

Because PrAlGe was not selected to maximize higher-order torques, our results should be viewed as a *proof of principle*. The essential switching mechanism is not specific to this material but follows directly from the angu-

lar dependence of the vector spherical harmonics expansion. The dominance of the $\text{Im } \mathbf{Y}_{5,5}^D$ harmonic in PrAlGe provides one microscopic realization of this mechanism, but the toy-model phase diagrams show that many other combinations of higher-order harmonics can also generate the required fixed-point structure. This suggests that materials with cleaner low-energy electronic structure, reduced multiband complexity, and tunable control over the balance between conventional and higher-order torques, such that higher-order harmonics remain comparable in magnitude to the lowest-order terms while the overall torque amplitude is large enough to keep the required electric fields moderate, may provide even more favorable platforms. In addition, materials with smaller anisotropy fields would allow the same fixed-point mechanism to operate at reduced electric fields, trading a longer switching timescale for improved experimental accessibility without altering the underlying dynamics.

Experimentally, the mechanism predicts several clear signatures: (i) nontrivial angular dependence of the spin-orbit torque beyond the standard $\mathbf{p} \times \mathbf{m}$ and $\mathbf{m} \times (\mathbf{p} \times \mathbf{m})$ forms; (ii) relaxation toward stable opposite-hemisphere fixed points under finite electric field without breaking any in-plane mirror symmetries; and (iii) reversible switching using electric field pulses of either polarity, with trajectories that access symmetry-related fixed points. These features distinguish higher-order-driven switching from conventional symmetry-breaking schemes and may be accessible in optical pump-probe measurements, ultrafast Hall-based torque probes, or spin-torque ferromagnetic resonance experiments.

We also note that strong spin-orbit torques can modify the electronic topology itself. When the applied electric field rotates the magnetization away from its equilibrium orientation, the rotation symmetries that make the pairs of Weyl nodes energy degenerate may no longer be preserved (See Appendix F). Thus, a finite electric field can shift the Weyl-node positions in both momentum and energy, dynamically tuning the Berry curvature landscape during the switching process. Although this effect is not the origin of the deterministic switching identified here, it provides an additional experimentally accessible signature of higher-order torques and may offer another route to materials optimization: materials in which the Weyl nodes are close to the Fermi level or highly sensitive to electric-field-induced spin tilting may exhibit an even stronger higher-order torque response.

Future work may focus on identifying materials in which higher-order harmonics are intrinsically enhanced—such as noncentrosymmetric semimetals with simpler band topology, magnetic altermagnets with strong anisotropic Berry curvature responses [44], or engineered heterostructures where symmetry and band filling can be tuned. The toy-model framework introduced here provides a systematic strategy for such a search by connecting crystalline symmetry, torque harmonics, and switching phase diagrams. As a whole, our findings establish higher-order spin-orbit torques as an un-

derexplored but powerful route for electric-field control of magnetization.

VII. ACKNOWLEDGMENT

The authors would like to acknowledge Dr. J Shi and Dr. R Islam for their assistance and helpful discussions throughout this project. The work done at University of Alabama at Birmingham is supported by the National Science Foundation under Grant No. OIA-2229498, UAB internal startup funds, and UAB Faculty Development Grant Program, Office of the Provost. The authors gratefully acknowledge the resources provided by the University of Alabama at Birmingham IT-Research Computing group for high performance computing (HPC) support and CPU time on the Cheaha compute cluster. This work used Stampede3 at Texas Advanced Computing Center through allocation PHY250049 from the Advanced Cyberinfrastructure Coordination Ecosystem: Services & Support(ACCESS) program, which is supported by U.S. National Science Foundation grants #2138259, #2138286, #2138307, #2137603, and #2138296.

Appendix A: Symmetry Analysis

This appendix supplements Sec. II by outlining the vector spherical harmonics (VSH) expansion used to derive the symmetry-allowed forms of spin-orbit torque (SOT) in systems with C_{4z} rotational symmetry. The methodology closely follows Ref. [26]. For a magnetization direction $\hat{\mathbf{m}} = (\sin \theta \cos \phi, \sin \theta \sin \phi, \cos \theta)$, the vector spherical harmonics components are defined in terms of scalar spherical harmonics $Y_{lm}(\hat{\mathbf{m}})$ as

$$\mathbf{Y}_{lm}^D(\hat{\mathbf{m}}) = \frac{\nabla_{\hat{\mathbf{m}}} Y_{lm}(\hat{\mathbf{m}})}{\sqrt{l(l+1)}}, \quad (A1)$$

$$\mathbf{Y}_{lm}^F(\hat{\mathbf{m}}) = \frac{\hat{\mathbf{m}} \times \nabla_{\hat{\mathbf{m}}} Y_{lm}(\hat{\mathbf{m}})}{\sqrt{l(l+1)}}. \quad (A2)$$

Both \mathbf{Y}_{lm}^D and \mathbf{Y}_{lm}^F are orthogonal to $\hat{\mathbf{m}}$ and are classified as dampinglike and fieldlike respectively based on their roles in spin dynamics governed by LLG equation. The fieldlike \mathbf{Y}_{lm}^F terms are curl-free and correspond to gradients of scalar fields, while the dampinglike terms are generated from their curls and can be written as $\hat{\mathbf{m}} \times \mathbf{Y}_{lm}^F$.

Time-reversal symmetry (TRS) imposes constraints on which harmonics can appear. As summarized in Table II, \mathbf{Y}_{lm}^D is odd (even) under TRS for even (odd) l , while \mathbf{Y}_{lm}^F is even (odd) under TRS for even (odd) l .

The SOT can be expressed in linear response as

$$\mathcal{T}_{\hat{\mathbf{E}}}(\hat{\mathbf{m}}) = \boldsymbol{\tau}_{\hat{\mathbf{E}}}(\hat{\mathbf{m}}) \mathbf{E}, \quad (A3)$$

	l even	l odd
\mathbf{Y}_{lm}^D	odd	even
\mathbf{Y}_{lm}^F	even	odd

TABLE II. Time-reversal symmetry properties of the vector spherical harmonics $\mathbf{Y}_{lm}^{D,F}$.

where the torkance tensor is expanded in the VSH basis:

$$\boldsymbol{\tau}_{\hat{\mathbf{E}}}(\hat{\mathbf{m}}) = \sum_{lm} \left[\mathbf{Y}_{lm}^D C_{lm}^D(\hat{\mathbf{E}}) + \mathbf{Y}_{lm}^F C_{lm}^F(\hat{\mathbf{E}}) \right]. \quad (\text{A4})$$

Here the coefficients $C_{lm}^{D,F}$ represent the contributions of the corresponding VSH terms to the torque.

For a system with C_{4z} rotational symmetry, the relevant symmetries include the fourfold rotation about $\hat{\mathbf{z}}$ together with mirror planes in both the xz and yz directions. The fourfold rotation ensures that the torkance is invariant when we perform a rotation angle $\gamma = \pi/2$ from $x(y)$ -axis [26]:

$$\begin{aligned} C_{lm}(\hat{\mathbf{x}}) e^{-im\gamma} &= C_{lm}(\hat{\mathbf{x}}) \cos \gamma + C_{lm}(\hat{\mathbf{y}}) \sin \gamma, \\ C_{lm}(\hat{\mathbf{y}}) e^{-im\gamma} &= -C_{lm}(\hat{\mathbf{x}}) \sin \gamma + C_{lm}(\hat{\mathbf{y}}) \cos \gamma. \end{aligned} \quad (\text{A5})$$

These equations require that only harmonics with $m = 4n \pm 1$ are symmetry-allowed. Terms with $m = 4n$ or $m = 4n+2$ are forbidden, since they acquire inconsistent phase factors under a 90° rotation and thus do not remain invariant. Consequently, the torque expansions for $\mathbf{E} \parallel \hat{\mathbf{x}}$ and $\mathbf{E} \parallel \hat{\mathbf{y}}$ involve the same set of harmonics ($m = 4n \pm 1$), differing only by the phase relation enforced by the C_{4z} rotation:

$$C_{l,4n\pm 1}(\hat{\mathbf{y}}) = \mp i C_{l,4n\pm 1}(\hat{\mathbf{x}}). \quad (\text{A6})$$

The mirror planes impose specific constraints on the allowed vector spherical harmonics. These mirror-plane constraints are summarized in Table III, which lists the allowed (l, m) values for the real and imaginary parts of $\mathbf{Y}_{lm}^{D,F}$. The coordinate system is chosen such that $\hat{\mathbf{x}} \parallel \mathbf{E}$, $\hat{\mathbf{z}} \parallel \hat{\mathbf{n}}$ (film normal), and $\hat{\mathbf{y}} = \hat{\mathbf{n}} \times \hat{\mathbf{E}}$. In practice, we work with real-valued vector spherical harmonics obtained from the real and imaginary parts of \mathbf{Y}_{lm} . This guarantees that all basis functions are real and orthonormal on the unit sphere. In this convention m runs from 0 to l , with $\text{Re } \mathbf{Y}_{lm}$ and $\text{Im } \mathbf{Y}_{lm}$ providing two independent real basis functions for each nonzero m . This is the reason why the mirror-plane constraints in Table III are expressed separately for the real and imaginary parts of $\mathbf{Y}_{lm}^{D,F}$.

By combining the mirror constraints in Table III with the time-reversal properties in Table II, we obtain the symmetry-allowed forms of the spin-orbit torque for $E \parallel \hat{\mathbf{x}}$, given in Eqs. 1 and 2 of the main text.

$$\begin{aligned} \boldsymbol{\tau}^{\text{even}}(\hat{\mathbf{x}}) = \sum_{l,m} & [C_{2l,4m\pm 1}^F \text{Re } \mathbf{Y}_{2l,4m\pm 1}^F \\ & + C_{2l+1,4m\pm 1}^D \text{Im } \mathbf{Y}_{2l+1,4m\pm 1}^D], \end{aligned} \quad (\text{A7})$$

Mirror plane	$\text{Re } \mathbf{Y}_{lm}^{D,F}$	$\text{Im } \mathbf{Y}_{lm}^{D,F}$
$\sigma_{\hat{\mathbf{E}}, \hat{\mathbf{n}}}$	l even	l odd
$\sigma_{\hat{\mathbf{p}}, \hat{\mathbf{n}}}$	$l+m$ odd	$l+m$ even
$\sigma_{\hat{\mathbf{p}}, \hat{\mathbf{E}}}$	m even	m even

TABLE III. Symmetry constraints on (l, m) imposed by different mirror planes. If multiple mirrors are present, their constraints combine.

$$\begin{aligned} \boldsymbol{\tau}^{\text{odd}}(\hat{\mathbf{x}}) = \sum_{l,m} & [C_{2l,4m\pm 1}^D \text{Re } \mathbf{Y}_{2l,4m\pm 1}^D \\ & + C_{2l+1,4m\pm 1}^F \text{Im } \mathbf{Y}_{2l+1,4m\pm 1}^F]. \end{aligned} \quad (\text{A8})$$

By utilizing Eq. A6, we obtain

$$\begin{aligned} \boldsymbol{\tau}^{\text{even}}(\hat{\mathbf{y}}) = \sum_{l,m} & [\pm C_{2l,4m\pm 1}^F \text{Im } \mathbf{Y}_{2l,4m\pm 1}^F \\ & \mp C_{2l+1,4m\pm 1}^D \text{Re } \mathbf{Y}_{2l+1,4m\pm 1}^D], \end{aligned} \quad (\text{A9})$$

$$\begin{aligned} \boldsymbol{\tau}^{\text{odd}}(\hat{\mathbf{y}}) = \sum_{l,m} & [\pm C_{2l,4m\pm 1}^D \text{Im } \mathbf{Y}_{2l,4m\pm 1}^D \\ & \mp C_{2l+1,4m\pm 1}^F \text{Re } \mathbf{Y}_{2l+1,4m\pm 1}^F]. \end{aligned} \quad (\text{A10})$$

Appendix B: Critical Field LLG Simulation

To demonstrate that the higher-order torque consistently drives magnetization to the same off-equator fixed point, and to confirm that this outcome is not merely coincidental, we conducted additional Landau-Lifshitz-Gilbert (LLG) simulations starting from multiple randomly chosen initial conditions near the easy-axis poles. As shown in Table IV, all tested initial magnetization directions consistently evolve to the same stable fixed point when higher-order torque contributions are sufficiently large (ratio = 0.4) shown in table IV. In contrast, with smaller higher-order torque contributions (ratio = 0.1) shown in table V, the magnetization is driven only to the equator, reflecting nondeterministic outcomes. These results confirm that the deterministic switching enabled by higher-order torques is robust and occurs systematically, provided the initial magnetization is away from the equatorial symmetry point.

Appendix C: Magnetization Dynamics Phase Diagrams for $\text{Im } \mathbf{Y}_{3,3}^D$ and $\text{Im } \mathbf{Y}_{5,5}^D$

Section III studies the magnetization dynamics of a toy model incorporating conventional terms with the addition of the higher-order term $\text{Im } \mathbf{Y}_{3,3}^F$. Utilizing Landau-Lifshitz dynamics, Fig. 5 (c) showed that this higher term allowed for deterministic switching when its contribution was large enough. Here we apply the same LLG-based analysis to two additional higher-order harmonics

θ	ϕ	final m_z
-0.490	3.543	-0.086
-0.358	3.277	-0.086
0.016	0.432	-0.086
-0.668	6.034	-0.086
0.679	3.038	-0.086
0.204	1.706	-0.086
-0.475	3.274	-0.086
0.173	2.244	-0.086
0.702	1.193	-0.086
-0.359	3.621	-0.086
0.521	2.767	-0.086

TABLE IV. LLG simulation results for $E = 0.8H_A$ and ratio = 0.4. Initial conditions ($-\pi/4 < \theta < \pi/4, 0 < \phi < 2\pi$) all converge to the same off-equator fixed point.

θ	ϕ	final m_z
-0.290	3.333	0
-0.244	2.526	0
-0.491	0.660	0
-0.553	1.092	0
0.611	4.502	0
0.013	4.000	0
0.556	0.263	0
-0.362	4.131	0
-0.196	6.122	0
0.459	4.361	0
0.424	1.825	0

TABLE V. LLG simulation results for $E = 0.8H_A$ and ratio = 0.1. All initial conditions converge to the equator, leading to nondeterministic outcomes.

that arise in the *ab initio* torques of PrAlGe, namely $\text{Im } \mathbf{Y}_{3,3}^D$ and $\text{Im } \mathbf{Y}_{5,5}^D$.

As shown in Fig. 7(a), the term $\text{Im } \mathbf{Y}_{3,3}^D$ does not produce deterministic switching but instead generates an extended oscillatory (precessional) regime. Such oscillatory dynamics can also be useful as nano-oscillators, in which the frequency can be tuned by varying the ratio of higher-order to conventional torque amplitudes [45].

Figure 7(b) presents the phase diagram for $\text{Im } \mathbf{Y}_{5,5}^D$, which is identified in Sec. IV as the dominant higher-order term responsible for deterministic switching in PrAlGe. In this case, a sufficiently large ratio of $\text{Im } \mathbf{Y}_{5,5}^D$ to the lowest-order torque components produces the same off-equator fixed-point structure as the toy model, enabling deterministic switching. The required ratio is larger than for the $\text{Im } \mathbf{Y}_{3,3}^F$ term considered in the main text, but the qualitative mechanism is the same.

Appendix D: First-Principle Calculation

PrAlGe is modeled using Vienna Ab initio Simulation Package utilizing a GGA+ U method. We utilize a $14 \times 14 \times 14$ Gamma-centered mesh and an energy cutoff of 500 eV. We implement a Hubbard U of 4 eV as done in literature [17] [19]. Both collinear and noncollinear

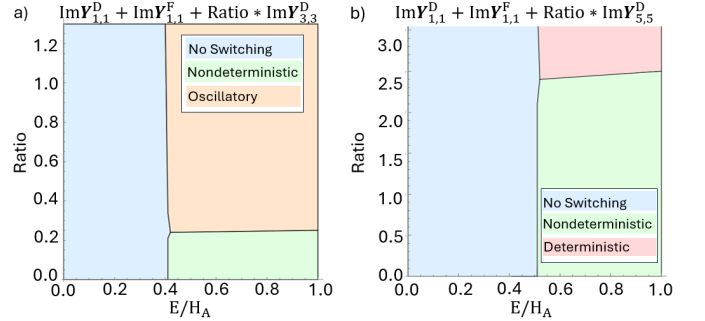


FIG. 7. Phase diagrams of magnetization dynamics for higher-order torque harmonics: (a) $\text{Im } \mathbf{Y}_{3,3}^D$ and (b) $\text{Im } \mathbf{Y}_{5,5}^D$.

calculations are performed. The k-path used to obtain the band structures in Figs. 3(c) and (d) follows the high symmetry points reported in Table VI.

Label	k_x	k_y	k_z
Γ	0.0000	0.0000	0.0000
Σ_0	-0.2710	0.2710	0.2710
N	0.0000	0.5000	0.0000
Σ	0.2710	0.7290	-0.2710
Z	0.5000	0.5000	-0.5000
X	0.0000	0.0000	0.5000

TABLE VI. High-symmetry k-points used as the path for the band structure of PrAlGe in fractional coordinates.

From the plane-wave calculation, we obtain a tight-binding Hamiltonian of the collinear calculation using Wannier90 [34]. The atomic orbital basis used are Ge: s, p ; Al: s, p ; Pr: d, f , and these are chosen from the density of states calculations and agree with atomic orbitals chosen in previous literature of this material [17] [19]. Now that a tight-binding Hamiltonian has been achieved, WannSymm [35] is then used to symmetrize the Hamiltonian.

Appendix E: Fitting at the Fermi energy

Spin-orbit torques were computed over a range of chemical potentials, as shown in Fig. 4. For completeness, we also provide the fitted vector spherical harmonics coefficients evaluated at the DFT Fermi level $\mu = 0$, summarized in Table VII.

Appendix F: Weyl Points

WannierTools [46] was used to identify Weyl points for the noncollinear tight-binding model derived from DFT, as well as the collinear tight-binding model with atomically added spin-orbit coupling (SOC).

Table VIII lists the seven independent Weyl points found in the noncollinear model. Accounting for crystal

$C_{1,1}^D$	$C_{3,3}^D$	$C_{5,1}^D$	$C_{5,3}^D$	$C_{5,5}^D$	$C_{7,1}^D$	$C_{2,1}^F$	$C_{4,3}^F$
-0.008	-0.006	-0.006	0.003	0.006	0.001	0.003	0.005

$C_{2,1}^D$	$C_{4,1}^D$	$C_{4,3}^D$	$C_{1,1}^F$	$C_{3,1}^F$	$C_{3,3}^F$
0.023	-0.001	-0.001	-0.026	-0.001	0.001

TABLE VII. Fitting coefficients for spin-orbit torque at the Fermi energy $\mu = 0$ eV. The upper table includes the time-reversal even terms and the lower table are the time-reversal odd. Terms smaller than 0.001 are excluded for brevity.

k_x (1/Å)	k_y (1/Å)	k_z (1/Å)	Energy (meV)
0.366	0.058	0.280	-8.1
0.287	0.245	0.054	28.9
0.236	0.291	0.048	31.1
0.013	0.688	0.391	46.5
0.039	0.381	0.289	50.4
0.230	0.309	0.001	50.9
0.416	0.254	0.004	69.6

TABLE VIII. Symmetry-inequivalent Weyl nodes for the noncollinear tight-binding Hamiltonian with magnetization along \hat{z} . Energies are measured relative to the Fermi level.

symmetries, these correspond to a total of 56 Weyl nodes in the Brillouin zone, consistent with earlier reports [17].

After including atomic SOC in the collinear tight-binding Hamiltonian, six independent Weyl nodes are obtained, listed in Table IX. The reduction from seven to six inequivalent nodes arises because two nearby Weyl points in the noncollinear case merge into one under the collinear+SOC treatment.

A direct comparison between the two models is presented in Table X. Most Weyl nodes in the noncollinear model map cleanly to those in the collinear+SOC model, with small momentum displacements $\Delta k \lesssim 0.05\text{--}0.13$ 1/Å. One noncollinear Weyl point ($k \approx 0.236, 0.291, 0.048$) merges with its neighbor after SOC is added, explaining the reduction in the number of inequivalent nodes. Overall, the two approaches yield a consistent Weyl topology, with only minor differences in precise energies and positions.

From these six independent Weyl points, a total of 48 symmetry-related Weyl points emerge due to the sys-

k_x (1/Å)	k_y (1/Å)	k_z (1/Å)	Energy (meV)
-0.002	0.644	0.412	-21.4
0.289	0.245	0.045	2.6
0.036	0.338	0.349	30.8
0.386	0.051	0.299	36.3
0.257	0.431	0.003	48.3
0.019	0.315	0.396	83.0

TABLE IX. Symmetry-inequivalent Weyl nodes for the collinear tight-binding Hamiltonian with atomic SOC. Energies are measured relative to the Fermi level.

Noncollinear			Collinear+SOC			Δk (1/Å)
k_x	k_y	k_z	k_x	k_y	k_z	
0.366	0.058	0.280	0.386	0.051	0.299	0.030
0.287	0.245	0.054	0.289	0.245	0.045	0.010
0.236	0.291	0.048	0.245	0.289	-0.045	0.010
0.013	0.688	0.391	-0.002	0.644	0.412	0.046
0.039	0.381	0.289	0.036	0.338	0.349	0.074
0.230	0.309	0.001	0.257	0.431	0.003	0.127
0.416	0.254	0.004	0.431	0.257	-0.003	0.017

TABLE X. Comparison of symmetry-inequivalent Weyl nodes in the noncollinear vs collinear+SOC models. Coordinates are given in reciprocal Cartesian units (1/Å). The last column reports the momentum displacement Δk between corresponding nodes.

tem's crystal symmetries. Specifically, the system's four-fold rotational symmetry around the z -axis (C_{4z}) generates three additional Weyl points from each independent one through 90° rotations in momentum space. Consequently, groups of four Weyl points share the same chirality.

To satisfy the Nielsen-Ninomiya theorem [47, 48], which demands zero net chirality in periodic crystal, each Weyl point must possess a partner with opposite chirality. This partner arises from the combined action of mirror symmetry about the yz -plane (σ_{yz}) and time-reversal symmetry. Mirror symmetry preserves momentum while reversing spin, thus reversing chirality. Conversely, time-reversal symmetry simultaneously reverses both spin and momentum, leaving chirality unchanged. Thus, the combination of mirror and time-reversal symmetry ensures each Weyl point has a partner of opposite chirality.

As a representative example, Table XI lists the full set of eight Weyl points (four pairs with opposite chirality) generated from the Weyl point located near the Fermi level at $\mathbf{k} = (0.245, 0.289, -0.045)$ with an energy of 2.6 meV.

k_x (1/Å)	k_y (1/Å)	k_z (1/Å)	Chirality	E (meV)
0.245	0.289	-0.045	1	2.6
-0.289	0.245	-0.045	1	2.6
-0.245	-0.289	-0.045	1	2.6
0.289	-0.245	-0.045	1	2.6
0.245	-0.289	0.045	-1	2.6
-0.289	-0.245	0.045	-1	2.6
-0.245	0.289	0.045	-1	2.6
0.289	0.245	0.045	-1	2.6

TABLE XI. Representative set of symmetry-generated Weyl nodes. The first four are related by C_{4z} and share identical chirality. The last four are obtained via σ_{yz} and time-reversal, yielding opposite chirality.

Once the magnetization is rotated to $\hat{\mathbf{m}} \parallel \hat{\mathbf{y}}$, C_{4z} symmetry of the $\hat{\mathbf{z}}$ -aligned state are lifted, and the Weyl nodes shift in both momentum and energy. Specifically, the set of eight energy-degenerate nodes at $\hat{\mathbf{m}} \parallel \hat{\mathbf{z}}$ splits into four energy-nondegenerate nodes; each of these generates a quartet of symmetry-related partners under the

operations that remain at $\hat{\mathbf{m}} \parallel \hat{\mathbf{y}}$ (notably σ_{xz} , $\sigma_{yz}\mathcal{T}$, and $C_{2z}\mathcal{T}$). A representative set of the four independent nodes is listed in Table XII. Relative to the $\hat{\mathbf{m}} \parallel \hat{\mathbf{z}}$ case, the energy shifts exceed ~ 35 meV and the momentum displacements are $\sim 0.02 \text{ \AA}^{-1}$ (typical).

k_x (1/ \AA)	k_y (1/ \AA)	k_z (1/ \AA)	Chirality	E (meV)
0.257	0.283	-0.035	1	33.4
-0.278	0.258	-0.037	1	-19.7
-0.241	-0.304	-0.059	1	-10.3
0.309	-0.238	-0.050	1	38.0

TABLE XII. Four *independent* Weyl nodes for $\hat{\mathbf{m}} \parallel \hat{\mathbf{y}}$ corresponding to the first four C_{4z} symmetry-equivalent nodes in Table XI. Each entry generates a fourfold set of symmetry partners related by the operations that remain at $\hat{\mathbf{m}} \parallel \hat{\mathbf{y}}$ (σ_{xz} , $\sigma_{yz}\mathcal{T}$, and $C_{2z}\mathcal{T}$). The corresponding partners share the same energy; chirality transforms according to the underlying symmetry (in particular, it is preserved under $C_{2z}\mathcal{T}$ and changes sign under the mirrors).

- [1] A. Manchon, J. Železný, I. M. Miron, T. Jungwirth, J. Sinova, A. Thiaville, K. Garello, and P. Gambardella, *Rev. Mod. Phys.* **91**, 035004 (2019).
- [2] J. Grollier, D. Querlioz, K. Y. Camsari, K. Everschor-Sitte, S. Fukami, and M. D. Stiles, *Nature Electronics* **3**, 360 (2020).
- [3] Q. Shao, P. Li, L. Liu, H. Yang, S. Fukami, A. Razavi, H. Wu, K. Wang, F. Freimuth, Y. Mokrousov, M. D. Stiles, S. Emori, A. Hoffmann, J. Akerman, K. Roy, J.-P. Wang, S.-H. Yang, K. Garello, and W. Zhang, *IEEE Transactions on Magnetics* **57**, 1 (2021).
- [4] A. Hoffmann, S. Ramanathan, J. Grollier, A. D. Kent, M. J. Rozenberg, I. K. Schuller, O. G. Shpyrko, R. C. Dynes, Y. Fainman, A. Frano, E. E. Fullerton, G. Galli, V. Lomakin, S. P. Ong, A. K. Petford-Long, J. A. Schuller, M. D. Stiles, Y. Takamura, and Y. Zhu, *APL Materials* **10**, 070904 (2022).
- [5] I. M. Miron, K. Garello, G. Gaudin, P.-J. Zermatten, M. V. Costache, S. Auffret, S. Bandiera, B. Rodmacq, A. Schuhl, and P. Gambardella, *Nature* **476**, 189 (2011).
- [6] L. Liu, C.-F. Pai, Y. Li, H. W. Tseng, D. C. Ralph, and R. A. Buhrman, *Science* **336**, 555 (2012).
- [7] D. C. Worledge, G. Hu, D. W. Abraham, J. Z. Sun, P. L. Trouilloud, J. Nowak, S. Brown, M. C. Gaidis, E. J. O'Sullivan, and R. P. Robertazzi, *Applied Physics Letters* **98**, 022501 (2011), <https://doi.org/10.1063/1.3536482>.
- [8] B. Dieny and M. Chshiev, *Rev. Mod. Phys.* **89**, 025008 (2017).
- [9] L. Liu, O. J. Lee, T. J. Gudmundsen, D. C. Ralph, and R. A. Buhrman, *Phys. Rev. Lett.* **109**, 096602 (2012).
- [10] D. MacNeill, G. M. Stiehl, M. H. D. Guimaraes, R. A. Buhrman, J. Park, and D. C. Ralph, *Nature Physics* **13**, 300 (2016).
- [11] F. Xue, C. Rohmann, J. Li, V. Amin, and P. Haney, *Phys. Rev. B* **102**, 014401 (2020).
- [12] I.-H. Kao, R. Muzzio, H. Zhang, M. Zhu, J. Gobbo, S. Yuan, D. Weber, R. Rao, J. Li, J. H. Edgar, J. E. Goldberger, J. Yan, D. G. Mandrus, J. Hwang, R. Cheng, J. Katoch, and S. Singh, *Nature Materials* **21**, 1029 (2022).
- [13] L. Wang, J. Xiong, B. Cheng, Y. Dai, F. Wang, C. Pan, T. Cao, X. Liu, P. Wang, M. Chen, S. Yan, Z. Liu, J. Xiao, X. Xu, Z. Wang, Y. Shi, S.-W. Cheong, H. Zhang, S.-J. Liang, and F. Miao, *Science Advances* **8**, eabq6833 (2022), <https://www.science.org/doi/pdf/10.1126/sciadv.abq6833>.
- [14] S. N. Kajale, T. Nguyen, N. T. Hung, M. Li, and D. Sarkar, *Science Advances* **10**, eadk8669 (2024), <https://www.science.org/doi/pdf/10.1126/sciadv.adk8669>.
- [15] F. Mahfouzi, R. Mishra, P.-H. Chang, H. Yang, and N. Kioussis, *Phys. Rev. B* **101**, 060405 (2020).
- [16] D. Go, F. Freimuth, J.-P. Hanke, F. Xue, O. Gomonay, K.-J. Lee, S. Blügel, P. M. Haney, H.-W. Lee, and Y. Mokrousov, *Phys. Rev. Res.* **2**, 033401 (2020).
- [17] G. Chang, B. Singh, S.-Y. Xu, G. Bian, S.-M. Huang, C.-H. Hsu, I. Belopolski, N. Alidoust, D. S. Sanchez, H. Zheng, H. Lu, X. Zhang, Y. Bian, T.-R. Chang, H.-T. Jeng, A. Bansil, H. Hsu, S. Jia, T. Neupert, and M. Z. Hasan, *Physical Review B* **97**, 10.1103/physrevb.97.041104 (2018).
- [18] B. Meng, H. Wu, Y. Qiu, C. Wang, Y. Liu, Z. Xia, S. Yuan, H. Chang, and Z. Tian, *APL Materials* **7**, 051110 (2019).
- [19] D. S. Sanchez, G. Chang, I. Belopolski, H. Lu, J.-X. Yin, N. Alidoust, X. Xu, T. A. Cochran, X. Zhang, Y. Bian, S. S. Zhang, Y.-Y. Liu, J. Ma, G. Bian, H. Lin, S.-Y. Xu, S. Jia, and M. Z. Hasan, *Nature Communications* **11**, 10.1038/s41467-020-16879-1 (2020).
- [20] D. Destraz, L. Das, S. S. Tsirkin, Y. Xu, T. Neupert, J. Chang, A. Schilling, A. G. Grushin, J. Kohlbrecher, L. Keller, P. Puphal, E. Pomjakushina, and J. S. White, *npj Quantum Materials* **5**, 5 (2020).
- [21] W. Liu, J. Zhao, F. Meng, A. Rahman, Y. Qin, J. Fan, L. Pi, Z. Tian, H. Du, L. Zhang, and Y. Zhang, *Physical Review B* **103**, 214401 (2021).
- [22] R. Yang, M. Corasaniti, C. C. Le, C. Yue, Z. Hu, J. P. Hu, C. Petrovic, and L. Degiorgi, *npj Quantum Materials* **7**, 5 (2022).
- [23] O. K. Forslund, X. Liu, S. Shin, C. Lin, M. Horio, Q. Wang, K. Kramer, S. Mukherjee, T. Kim, C. Cacho, C. Wang, T. Shang, V. Ukleev, J. S. White, P. Puphal, Y. Sassa, E. Pomjakushina, T. Neupert, and J. Chang, *Phys. Rev. Lett.* **134**, 126602 (2025).
- [24] K. Garello, I. M. Miron, C. O. Avci, F. Freimuth, Y. Mokrousov, S. Blügel, S. Auffret, O. Boulle, G. Gaudin, and P. Gambardella, *Nature Nanotechnology* **8**, 587 (2013).
- [25] K. D. Belashchenko, A. A. Kovalev, and M. van Schilfgaarde, *Phys. Rev. B* **101**, 020407 (2020).
- [26] F. Xue, M. D. Stiles, and P. M. Haney, *Phys. Rev. B* **108**, 144422 (2023).
- [27] O. Johansen, V. Risinggård, A. Sudbø, J. Linder, and A. Brataas, *Phys. Rev. Lett.* **122**, 217203 (2019).
- [28] W. Fang, E. Schwartz, A. A. Kovalev, and K. D. Belashchenko, *Journal of Physics: Condensed Matter* **37**, 155801 (2025).
- [29] J. Slonczewski, *Journal of Magnetism and Magnetic Materials* **159**, L1 (1996).
- [30] S. L. Dudarev, G. A. Botton, S. Y. Savrasov, C. J. Humphreys, and A. P. Sutton, *Phys. Rev. B* **57**, 1505 (1998).
- [31] G. Kresse and J. Furthmüller, *Phys. Rev. B* **54**, 11169 (1996).
- [32] P. E. Blöchl, *Physical Review B* **50**, 17953 (1994).
- [33] G. Kresse and D. Joubert, *Physical Review B* **59**, 1758 (1999).
- [34] A. A. Mostofi, J. R. Yates, G. Pizzi, Y.-S. Lee, I. Souza, D. Vanderbilt, and N. Marzari, *Computer Physics Communications* **185**, 2309 (2014).
- [35] G.-X. Zhi, C. Xu, S.-Q. Wu, F. Ning, and C. Cao, *Computer Physics Communications* **271**, 108196 (2022).
- [36] K. Kurita and T. Koretsune, *Phys. Rev. B* **102**, 045109 (2020).
- [37] T. A. Tartaglia, J. N. Tang, J. L. Lado, F. Bahrami, M. Abramchuk, G. T. McCandless, M. C. Doyle, K. S. Burch, Y. Ran, J. Y. Chan, and F. Tafti, *Science Advances* **6**, eabb9379 (2020), <https://www.science.org/doi/pdf/10.1126/sciadv.abb9379>.
- [38] F. Freimuth, S. Blügel, and Y. Mokrousov, *Phys. Rev. B* **90**, 174423 (2014).
- [39] F. Mahfouzi and N. Kioussis, *Phys. Rev. B* **97**, 224426 (2018).

- [40] K. D. Belashchenko, A. A. Kovalev, and M. van Schilfgaarde, *Phys. Rev. Materials* **3**, 011401 (2019).
- [41] R. Skomski and D. J. Sellmyer, *Journal of Rare Earths* **27**, 675 (2009).
- [42] P. Puphal, C. Mielke, N. Kumar, Y. Soh, T. Shang, M. Medarde, J. S. White, and E. Pomjakushina, *Phys. Rev. Mater.* **3**, 024204 (2019).
- [43] W. Liu, J. Zhao, F. Meng, A. Rahman, Y. Qin, J. Fan, L. Pi, Z. Tian, H. Du, L. Zhang, and Y. Zhang, *Phys. Rev. B* **103**, 214401 (2021).
- [44] L. Šmejkal, J. Sinova, and T. Jungwirth, *Phys. Rev. X* **12**, 040501 (2022).
- [45] F. Xue and P. M. Haney, *Phys. Rev. B* **104**, 224414 (2021).
- [46] Q. Wu, S. Zhang, H.-F. Song, M. Troyer, and A. A. Soluyanov, *Computer Physics Communications* **224**, 405 (2018).
- [47] H. Nielsen and M. Ninomiya, *Physics Letters B* **130**, 389 (1983).
- [48] N. P. Armitage, E. J. Mele, and A. Vishwanath, *Rev. Mod. Phys.* **90**, 015001 (2018).